

# Source Characteristics of the 2016 Meinong ( $M_L$ 6.6), Taiwan, Earthquake, Revealed from Dense Seismic Arrays: Double Sources and Pulse-like Velocity Ground Motion

by Yen-Yu Lin,<sup>\*</sup> Te-Yang Yeh,<sup>†</sup> Kuo-Fong Ma, Teh-Ru Alex Song, Shiann-Jong Lee, Bor-Shouh Huang, and Yih-Min Wu

**Abstract** The 5 February 2016, Meinong, Taiwan, earthquake brought extensive damage to nearby cities with significant pulse-like velocity ground motions. In addition to the spatial slip distribution determination using filtered strong-motion data, we show that, with the advantage of the densely distributed seismic network as a seismic array, we can project the earthquake sources (asperities) directly using nearly unfiltered data, which is crucial to the understanding of the generation of the pulse-like velocity ground motions. We recognize that the moderate but damaging  $M_L$  6.6 Meinong earthquake was a composite of an  $M_w$  5.5 foreshock and an  $M_w$  6.18 mainshock with a 1.8–5.0 s time delay. The foreshock occurred at the hypocenter reported by the official agency, followed by the mainshock with a centroid located at 12.3 km to the north-northwest of the hypocenter and at a depth of 15 km. This foreshock–mainshock composition is not distinguishable in the finite-fault inversion because it filtered the seismic data to low frequencies. Our results show that the pulse-like velocity ground motions are mainly attributed to the source of mainshock with its directivity and site effects, resulting in the disastrous damages in the city of Tainan. Although finite-fault inversion using filtered seismic data for spatial slip distribution on the fault has been a classic procedure in understanding earthquake rupture processes, using a dense seismic network as a seismic array for unfiltered records helps us delineate the earthquake sources directly and provide more delicate information for future understanding of earthquake source complexity.

*Electronic Supplement:* Figures of waveform comparisons.

## Introduction

A moderate  $M_L$  6.6 earthquake struck southern Taiwan on 5 February 2016. It was the largest inland earthquake in Taiwan causing heavy damage since the 1999  $M_w$  7.6 Chi-Chi earthquake. According to the Central Weather Bureau's (CWB) official agency report, the earthquake occurred at location E120.5438°, N22.9220°, with a focal depth of 14.6 km, in the district of Meinong of the city of Kaohsiung (Fig. 1). This event caused 117 casualties, 551 injuries, and 412 collapsed and damaged buildings. Most of the destruction was located near the city of Tainan rather than the epicenter, the Meinong area (Figs. 1 and 2). Figure 2 shows the distribution

of peak ground acceleration (PGA) and peak ground velocity (PGV) with the seriously damaged buildings (squares), which confirmed that the largest shaking and velocity region was very close to the city of Tainan. The damages and fatalities caused by this moderate-size earthquake with moderate focal depth surprised the community. It requires further attention to understand future seismic hazards.

Seismologists commonly determine source characteristics for moderate-to-large earthquakes by the finite-fault inversion technique. They assume a fault plane based on an obtained focal mechanism and calculate Green's functions for geophysical records (e.g., seismic waveforms) on each subfault within the entire fault plane. Thus, they can solve for the slip-time history at all the subfaults on the fault plane. Because of the limitation of the velocity structure, only low-frequency geophysical records ( $< 0.5$  Hz) are applied in the finite-fault

<sup>\*</sup>Now at Seismological Laboratory, California Institute of Technology, 1200 East California Boulevard, MS 252-21, Pasadena, California 91125.

<sup>†</sup>Now at Department of Geological Sciences, San Diego State University, 5500 Campanile Drive, San Diego, California 92182.

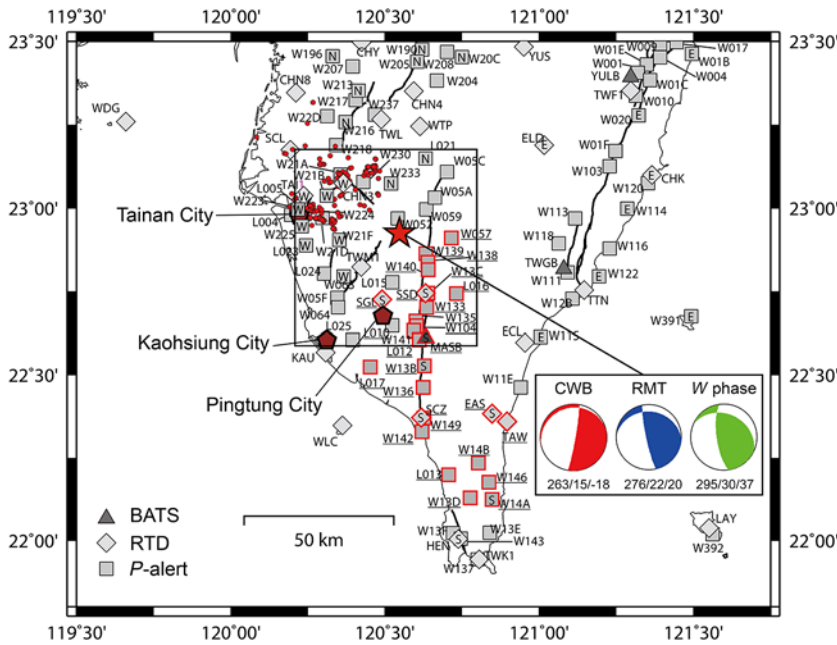


**Figure 1.** Map view of the Meinong earthquake epicenter, nearby metropolitan cities, and seismic station distribution. The star is the epicenter reported by the Central Weather Bureau (CWB). The solutions of focal mechanism from the first motion (CWB), real-time moment tensor (RMT) inversion, and *W*-phase inversion (*W* phase) are shown. Pentagons represent three major cities in southern Taiwan. Triangles, diamonds, and squares indicate the stations of the Broadband Array in Taiwan for Seismology (BATS), Real-Time Data (RTD), and *P*-alert, respectively. The stations labeled with an underline are those used for displaying the travel-time curve in Figure 3. The station marked by S, W, E, and N are for the layouts of the stations in the south, west, east, and north, respectively, in Figure 4. The large square reveals the area in Figure 5. The circles demonstrate seriously damaged buildings due to the Meinong earthquake. The lines reveal surface tracks for known faults in southern Taiwan. The color version of this figure is available only in the electronic edition.

inversion. This explains why the source characteristics of the Meinong earthquake have been determined using low-frequency geophysical records (e.g., seismic waveforms and Global Positioning System [GPS] records). Lee *et al.* (2016) estimated the focal mechanism by the real-time moment tensor (RMT) inversion technique and determined the coseismic slip characteristics by a joint-inversion procedure that considered teleseismic, local strong-motion records, with frequency bands lower than 0.33 Hz (3 s), and GPS data. Kanamori *et al.* (2016) obtained a coseismic slip model through a finite-fault inversion technique using the teleseismic records in frequency bands from 2 to 30 s. Their results indicated that the centroid of the Meinong earthquake was located ~10 km north-northwest of the epicenter reported by the CWB. They both concluded that the unexpected large ground motions that appeared in the city of Tainan were because of the combination of strong directivity, radiation pattern, and site amplification. According to their moment tensor solutions, the Meinong earthquake could have ruptured either the northwest–south-east low-angle plane or the north–south high-angle plane (Fig. 1). They preferred the low-angle plane with a strike-slip mechanism.

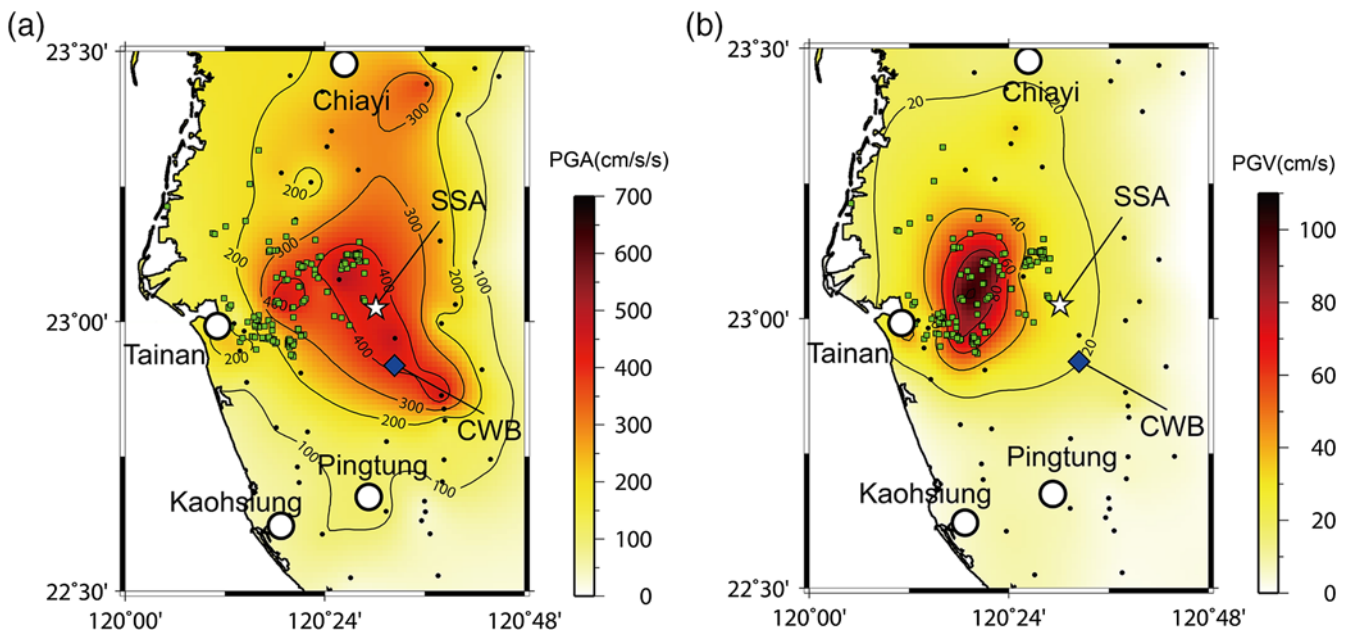


**Figure 2.** The distribution of the peak ground acceleration (PGA) and peak ground velocity (PGV). The damaged buildings and the *P*-alert stations are shown in squares and dots, respectively. The star and diamond are the locations of the mainshock centroid (source-scanning algorithm [SSA]) and epicenter (CWB), respectively. The color version of this figure is available only in the electronic edition.

Furthermore, [Jian \*et al.\* \(2017\)](#) analyzed high-frequency  $P$ -wave (0.5–1.5 Hz) teleseismic records for dense seismic networks in Europe and Australia and used a backprojection technique tracking the details of the rupture process. Their result indicated a rupture pattern similar to the results from the finite-fault inversions, going from the CWB epicenter to the northwest with an average rupture speed of 2.4 km/s.

Since 2013, Taiwan has operated an onsite  $P$ -alert earthquake early warning (EEW) system that has functioned well in alerting residents about local events ([Wu \*et al.\*, 2013](#)). The  $P$ -alert system (~600 stations as of 2017) uses low-cost strong-motion sensors that are typically installed on the first or second floor of elementary schools in Taiwan. It was a surprise that this low-cost strong-motion sensor also records high-quality strong-motion waveforms. We demonstrate the capability of these densely populated stations as well as other free-field stations, mainly from the  $P$ -alert system (see [Wu \*et al.\*, 2016](#), for more details) and use them as a seismic array to study the source of the Meinong earthquake. This dense seismic array allows us to study the earthquake without distortion from filtering the data. We are thus able to untangle the  $M_L$  6.6 Meinong earthquake as an event doublet, with an  $M_w$  5.5 foreshock a few seconds ahead of the  $M_w$  6.18 mainshock, in a blind fault system, using a source-scanning algorithm (SSA) technique. The close-in large short-duration velocity pulses generated by the single source of the  $M_w$  6.18 mainshock are what caused severe damage to the city of Tainan and the nearby region. This is typically referred to, in earthquake engineering, as the pulse-like velocity ground motion ([Hall \*et al.\*, 1995](#); [Heaton \*et al.\*, 1995](#)).

The pulse-like velocity ground motion is often characterized by a pulse wave of 1–2 s period with large amplitudes, causing tremendous damages to buildings ([Heaton \*et al.\*, 1995](#)). It is believed to be caused by a near-fault forward-directivity effect ([Somerville \*et al.\*, 1997](#); [Somerville, 2003](#); [Baker, 2007](#); [Shahi and Baker, 2011](#)). The collapse of a high-rise building that caused 115 deaths, and that of numerous other buildings in the western area of the Meinong earthquake, brought attention to the generation of the pulse-like velocity ground motion that was considerably responsible for the damage. The pulse-like velocity ground motion observed in the 1994 Northridge and 1995 Kobe earthquakes has been shown to have significant impact on earthquake hazards. The velocity pulse appears to be important for earthquake engineering because, when coupled with a large displacement peak, it could seriously damage buildings ([Hall \*et al.\*, 1995](#)). [Cox and Ashford \(2002\)](#) analyzed the near-field records from 15 large earthquakes. They summarized that the conditions for producing a large velocity pulse include (1) the earthquake is larger than  $M_w$  6.0; (2) the site is close to the fault, within 10 km; and (3) the rupture propagates toward the site. The generation of the pulse-like velocity ground motion of the 2016 Meinong earthquake is intriguing, because the observed pulse-like velocity ground motions were not identified as either near the fault or close to the hypocenter from rapid spatial slip distribution. The

in-depth examination of waveforms from the dense seismic network allows us to decipher the generation of the pulse-like velocity ground motion. Despite the fact that the dense  $P$ -alert seismic array was originally designed for EEW purposes, here we demonstrate how these high-quality recordings retrieved by the low-cost instruments greatly help us understand earthquake source complexity.

## Data

We analyze seismic waveforms from three seismic networks in Taiwan: (1) the Broadband Array in Taiwan for Seismology (BATS), operated by the Institute of Earth Science (IES), Academia Sinica, Taiwan; (2) the Real-Time Data (RTD) network, managed by the CWB; and (3) the  $P$ -alert network, operated by National Taiwan University. The instruments of the RTD and  $P$ -alert networks were accelerometers, and the instrument response was flat between 0.07 and 10 Hz. In the BATS network, both broadband seismometers and accelerometers were deployed in the same locations. The sampling rate was 100 samples per second for all stations. Clocks on the instruments for BATS and RTD were calibrated by GPS, and those for  $P$ -alert were done by Network Time Protocol through the Internet. Because the purpose of the present study is to understand the source process from nearby stations, we selected only the stations in southern Taiwan (latitude < N23.5°) with good azimuthal coverage ([Fig. 1](#)), including three stations from BATS (triangles), 29 from RTD (diamonds), and 91 from  $P$ -alert (squares), giving 123 stations in total. We discard records with drifting noise or saturation. Although the  $P$ -alert network is not made up of free-field stations, a test on the performance of this system against free-field stations shows almost no amplification and waveform distortion with respect to the recordings in the free-field stations. This could also be seen in [Figures 3 and 4](#) for the good correlation of the  $P$ -alert strong-motion data to those from free-field stations, such as those in BATS and RTD.

## Identification of Two Sources from the Waveform Travel-Time Curve

To determine the far-field term of the earthquakes, we obtain displacement waveforms from the acceleration records by double integrations. To avoid drifting during the integrations, we apply a zero-phase high-pass filter with a corner of 0.1 Hz to the data. We display the displacement record section against the epicenter and the origin time of the Meinong earthquake determined from the CWB report. Three-component record sections, including stations in the south (labeled with an underline in [Fig. 1](#)), are shown in [Figure 3a–c](#), for vertical ( $Z$ ), north ( $N$ ), and east ( $E$ ) components, respectively. To examine the waveforms from travel-time curves, we calculate the theoretical  $P$ - and  $S$ -wave arrival times ( $P_1$  and  $S_1$  phases as  $T_1$  and  $T_2$  markers shown in [Fig. 3](#)) from the hypocenter reported by the CWB using a

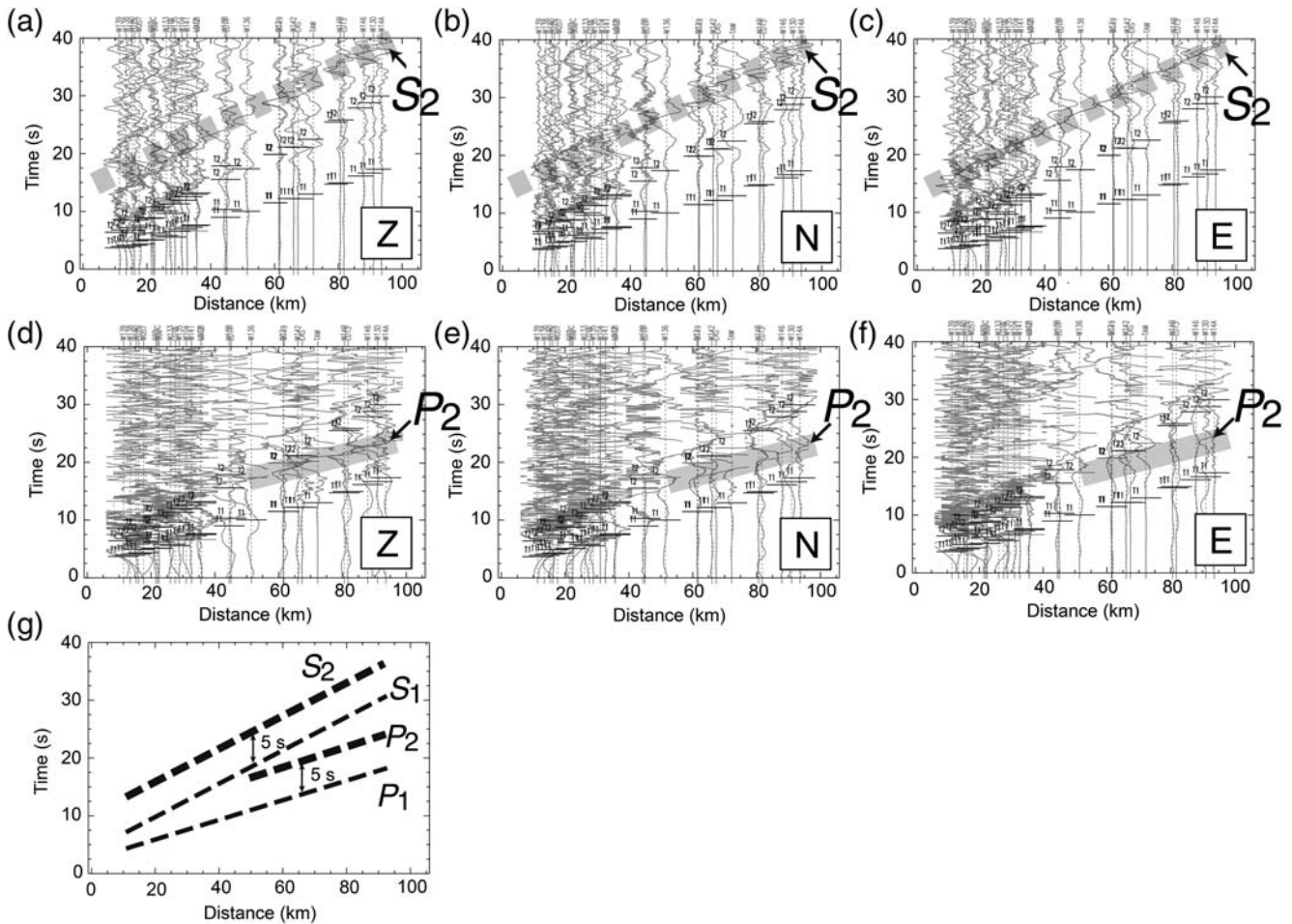


**Figure 3.** (a–c) The record sections of the vertical and the two horizontal components from the southern stations labeled with an underline mentioned in Figure 1. The amplitudes of each trace are normalized by the maximum amplitude. The moveout of  $S_2$  is revealed by the gray dashed lines. (d–f) The same record sections in which each trace only shows up to 20% of the maximum amplitude to demonstrate  $P$  waves clearly. The  $P_2$  phases are marked by the solid gray lines. The T1 and T2 markers are the  $P$ - and  $S$ -wave arrival times calculated by the H14-3D model ( $P_1$  and  $S_1$  phases). (g) The picked travel-time curves of  $P$ - and  $S$ -wave pairs for the foreshock and the mainshock are shown in thin and thick dashed lines, respectively.

Taiwan 3D velocity model (H14-3D) of Huang *et al.* (2014). This velocity model has a near-surface shallow velocity structure constrained from drilling logging data to provide a more reliable velocity layer near the surface.

We observe that obvious, stronger, and lower-frequency phases appear  $\sim 5.0$  s after the  $S_1$  phases in the record sections (Fig. 3a–c). The apparent velocity of these phases is similar to the velocity of the  $S_1$  phases, suggesting that these phases propagate by  $S$ -wave velocity. We call this phase  $S_2$  in the following study. Similarly, we identify clear and longer-period phases (called  $P_2$ ) propagating at the  $P$  wavespeed (Fig. 3d–f) that appears  $\sim 5.0$  s after the  $P_1$  phases between the  $P_1$  and  $S_1$  phases. The moveout of picked arrival times for  $P_1$ ,  $P_2$ ,  $S_1$ , and  $S_2$  phases is shown in Figure 3g. Because the delay times ( $\sim 5.0$  s) of  $P_2$ – $P_1$  and  $S_2$ – $S_1$  pairs are so similar, it is very likely that the  $P_2$ – $S_2$  pair is attributed to another seismic source located somewhere else, rather than to the source at the hypocenter with a few seconds of delay time. For the difference in amplitude and origin time of these

two sources, we separate them from the Meinong earthquake rupture history and refer to the first source as the foreshock and the second source as the mainshock.

### Location of the Mainshock

Because the temporal separation between the two events was only several seconds, it is challenging to detect both events for the routine determination of earthquake location and magnitude, such as in the CWB report, which is based on information from less-populated seismic stations. We improve an SSA technique described in Kao and Shan (2004) to determine the location of the mainshock to resolve the complexity in  $P_2$  and  $S_2$  pickings. The SSA method was successfully applied to the locations of events with ambiguous first arrivals, such as the distribution of the episodic tremor and slip sequence determination in the northern Cascadia subduction zone (Kao and Shan, 2004) and the rapid identification of fault planes for earthquakes (Kao and Shan,

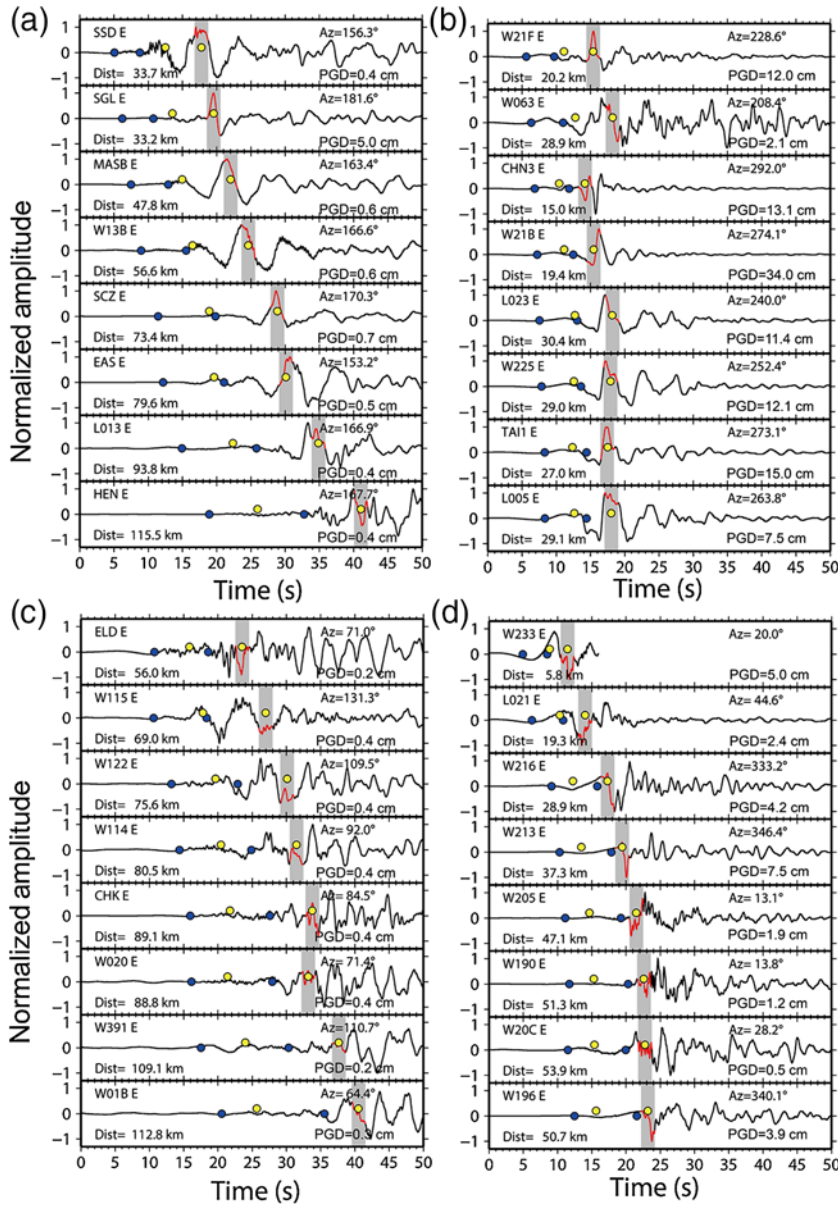


**Figure 4.** Displacement waveforms of the east component of the stations in the (a) south, (b) west, (c) east, and (d) north. The dark circles indicate the  $P_1$  and  $S_1$  phases for the foreshock. The light circles are  $P_2$  and  $S_2$  phases for the mainshock. The time window marked in gray is the contribution of the  $S_2$  phase in each trace. The station name, distance, and azimuth are indicated on the traces. The color version of this figure is available only in the electronic edition.

2007; Kao *et al.*, 2008). It was also used for the delineation of source characteristics of earthquake doublets (Kan *et al.*, 2010), near-real-time epicentral determination of landslides (Kao *et al.*, 2012), and location estimation of the earthquakes observed by the ocean-bottom seismometers network offshore southern Taiwan (Liao *et al.*, 2012).

We slightly modify the current SSA method to simultaneously determine the most likely location of the mainshock as well as its uncertainty. The idea is to convert each displacement waveform to a probability density function (PDF), representing the distribution of seismic energy as a

function of time. To convert seismic waveforms into PDFs, we integrate acceleration records to displacement, apply a zero-phase high-pass filter with a corner of 0.1 Hz to avoid drifting, square the amplitude to make it positive, and scale the squared amplitudes so that the area beneath the function is one. Because our goal is to determine the location of the source that caused the large pulse in horizontal components, only east–west and north–south components are used in the following analysis.

The SSA is a grid-search method for determining optimal distribution of the source location based on the seismic waveforms. The SSA method described in Kao and Shan (2004) stacked all normalized waveforms and calculated the brightness of an assumed source point ( $\eta$ ) at a specific delay time ( $\tau$ ). The source location was determined to be in the maximum brightness location. In the modified version of SSA, we compute probabilities of a proposed source location and delay time from each PDF by summing the amplitudes in the predicted time window. It is noted that the predicted time window has a certain width so that it can accommodate the errors from inaccurate travel-time prediction. We define the brightness function for the modified SSA as the product of the probabilities computed from all the PDFs, which is equivalent to the likelihood of the proposed model

$$\text{br}(\eta, \tau) = \prod_{n=1}^N \sum_{m=-M}^M |P_n(\tau + t_{\eta n} + mdt)|, \quad (1)$$

in which  $P_n$  is the PDF converted from seismic trace  $n$ ;  $t_{\eta n}$  is the predicted travel time for  $S$  wave from point  $\eta$  to station  $n$ ;  $2M$  is the number of points within the time window centered around the predicted arrival time; and  $dt$  is the sampling interval.

We calculate the brightness from the records of all stations in the Data section except from the stations with bad data quality, such as from disconnection due to large shaking, which results in 113 stations in total. We search the potential source area from longitude E120.20° to 120.80° and latitude N22.60° to 23.20° with a 0.025° interval in both directions. The depth grids are from 5.0 to 30.0 km with a 2.5 km interval. The delay times range from 0.0 to 10.0 s with a 0.05 s interval. The predicted  $S$ -wave travel times  $t_{\eta n}$  are calculated based on the H14-3D model. According to the

residuals of  $S$ -wave arrival times in the model (Huang *et al.*, 2014), we consider a time window of  $\pm 1.0$  s ( $M = 100$ ) when computing the probabilities. As a result, we derived a multidimensional likelihood function that could be considered as an approximation of the posterior probability distribution of the model parameters. The maximum-likelihood centroid location and delay time of the mainshock are therefore determined.

To test the resolution of the improved SSA method, we produce pulse-like displacement records with a 1.5 s duration representing  $P$  and  $S$  waves at all stations with a 5.0 s centroid delay. The arrivals of  $P$  and  $S$  waves are predicted based on the H14-3D model; note that we add uniformly distributed random travel-time residuals ranging in  $\pm 1.0$  s. 20% maximum amplitude random noises are considered in the synthetics. Following the same data processing we mentioned previously, the test results indicate that this method can determine the source location and timing accurately (Fig. S1, available in the electronic supplement to this article). We further compare the results analyzed by real data between the improved and original SSA methods. The results reveal that the improved SSA method indeed improves both spatial and temporal resolution compared with the original SSA method (Fig. S2).

The maximum probability in space of the mainshock centroid is determined to be at a location ( $E120.500^\circ$ ,  $N23.025^\circ$ ) that is 12.3 km north-northwest of the CWB epicenter where there is a blank zone of the aftershocks (Fig. 5a). The focal depth is 15 km, as shown in Figure 5b. Based on the location and the delay time of 5.3 s of the mainshock centroid estimated above, the corresponding  $P_1$ ,  $S_1$  and  $P_2$ ,  $S_2$  for the foreshock and mainshock are clearly identified accordingly from the waveforms in an east–west component for the stations in the south, west, north, and east (Fig. 4). These arrival pairs are consistent with the observations in the travel-time curve shown in Figure 3. The stations in the southern region show the most evidence of the corresponding  $P$ - and  $S$ -wave pairs for their backward direction to the foreshock and mainshock. Because of complex structures beneath the Central Range, the mainshock pulses become unclear at the predicted centroid times for some stations to the east.

We further compare the solutions of the Meinong earthquake location from different analyses based on different datasets—CWB,  $P$ -alert, RMT,  $W$  phase, and Global Centroid Moment Tensor (CMT)—shown in the open symbols in Figure 5a–b. This is firsthand information of the Meinong earthquake for the public. The solutions estimated by  $P$ -wave arrival-time information from the local networks, such as the CWB (the star) and  $P$ -alert (the diamond), distribute close to the CWB epicenter. However, the solutions determined by the waveform inversion techniques based on only teleseismic data (Global CMT) or regional records (RMT and  $W$  phase) are grouped in the northwest region, where the SSA technique located the mainshock. It suggests that the methods using the waveform inversion techniques or using teleseismic records have difficulty rec-

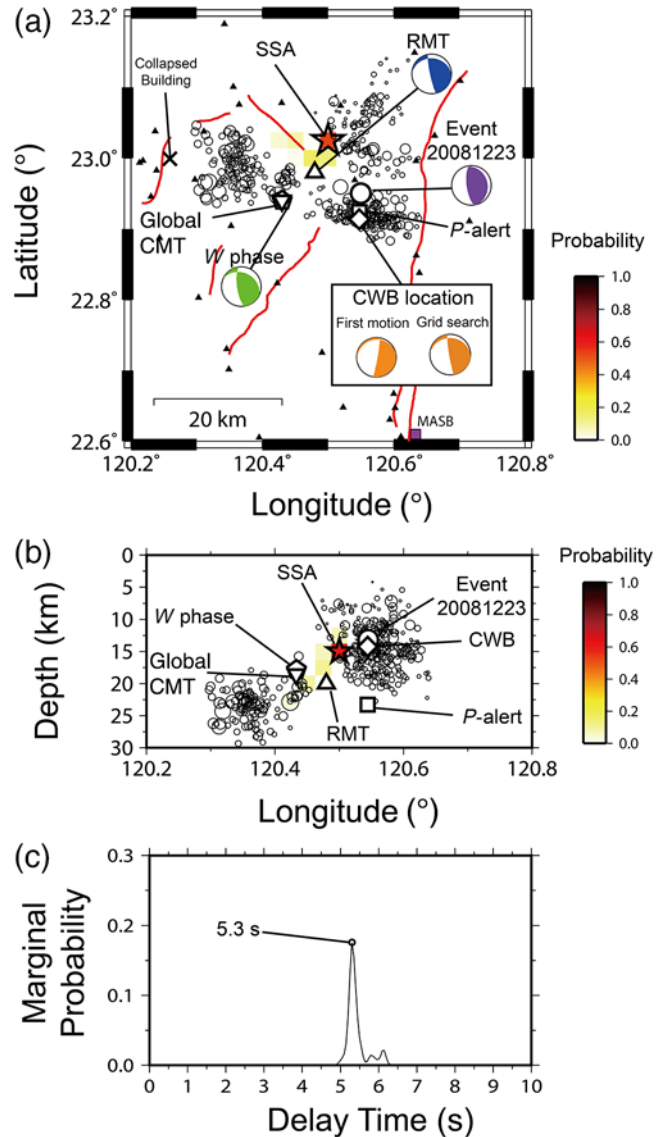


**Figure 5.** (a) The probabilities distribution of the mainshock centroid in the map view and (b) the east–west–depth profile. The color scale indicates the probability of the mainshock centroid in the location. The open diamond, square, triangle, inverse triangle, and pentagon reveal the solutions from the CWB,  $P$ -alert, RMT, Global Centroid Moment Tensor (CMT), and  $W$  phase, respectively. The circle is the location of the small earthquake (event from 23 December 2008; hereafter, E2008). The focal mechanisms of the  $W$  phase and RMT for the Meinong earthquake and for the E2008 earthquake are revealed. The comparison of the first-motion and grid-search solutions of the foreshock are shown. Station MASB and the fully collapsed building are marked in a square and  $\times$ , respectively. The solid triangles are the strong-motion stations used in the study. (c) Marginal probability of the delay time. The maximum probability is marked with an open circle in 5.3 s. The color version of this figure is available only in the electronic edition.

ognizing the event doublet because of the insufficiency of the frequency band in high frequencies, as we suggested earlier. The results from waveform inversion and teleseismic waveforms are mainly for the mainshock we identified in the present study.

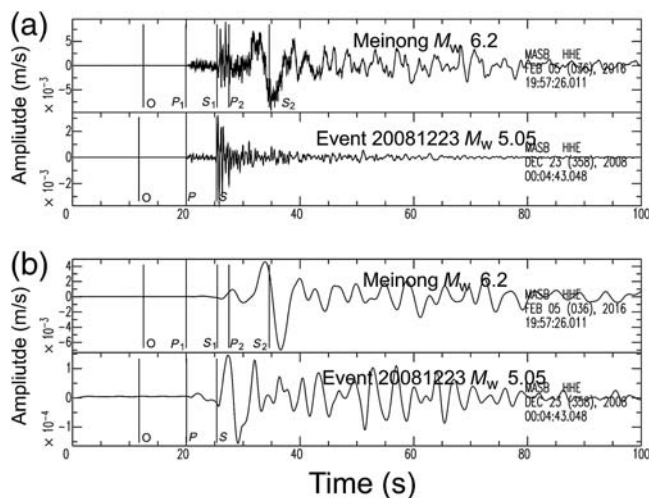


**Figure 6.** (a) Comparison of the east-component waveforms for the Meinong earthquake and the E2008 event ( $M_w$  5.05) from Station MASB. (b) The waveforms apply a low-pass filter of 0.33 Hz. The arrivals of the  $P_1$ ,  $S_1$ ,  $P_2$ , and  $S_2$  phases are indicated on the traces of the 2016 Meinong earthquake. The E2008 event's  $P$ - and  $S$ -wave arrivals are demonstrated on its traces.

In Figure 5c, we identify that the maximum probability of delay time for the mainshock centroid is at 5.3 s. Although the estimated delay time indicates a centroid delay of the mainshock compared to the origin time of the Meinong earthquake (the foreshock), it is challenging to determine the precise origin time of the mainshock. We calculate the centroid half-duration to be  $\sim 3.5$  s for an  $M_w$  6.18 earthquake, following the relation described by Duputel *et al.* (2013). Therefore, the origin-time difference between both events should be longer than 1.8 s. Because we knew that the mainshock location was in the north of the foreshock, the determined  $\sim 5.0$  s delay of  $P_2-P_1$  and  $S_2-S_1$  phases in the stations in the south in the Identification of Two Sources from the Waveform Travel-Time Curve section should include a longer propagating path and time than the source at the hypocenter. Therefore, the exact origin-time delay of the mainshock should be less than 5.0 s. We thus recognize that the origin time of the mainshock should be 1.8–5.0 s later than the foreshock.

### Magnitudes and Focal Mechanisms of the Foreshock and the Mainshock

The short separation in time (1.8–5.0 s) between both events makes it difficult to precisely identify the waveforms and estimate source parameters (e.g., magnitude and focal mechanism) for the buried event. In this section, we discuss using the waveforms from the southern stations (e.g., Station MASB) that have clear  $P_1$  and  $S_1$  phases to estimate the magnitude and focal mechanism of the foreshock.

To separate the foreshock signals from the waveforms, we compare the unfiltered velocity waveforms of Station MASB in the east component of the Meinong earthquake and

a nearby smaller earthquake, the  $M_w$  5.05 event from 23 December 2008 (hereafter, E2008), as shown in Figure 6a. The magnitude and the focal mechanism of the E2008 event were estimated by moment tensor inversion. The location of the E2008 earthquake and its focal mechanism, which is similar to that of the Meinong earthquake, are shown in Figure 5a. In Figure 6a, we mark the  $P_1$ ,  $S_1$ ,  $P_2$ , and  $S_2$  arrivals on the waveform of the Meinong earthquake and also show, for the reference, the  $P$ - and  $S$ -wave arrivals for the small earthquake on the records. All phases in the Meinong records are recognized clearly, except the  $P_2$  phase, which mixes with the  $S_1$  phase. The  $S_2$  phase with long-period signals appears significant, but it cannot be identified on the waveform of the small earthquake. This signal appears in velocity records recorded from both the accelerometer and broadband instrument, indicating that it was not due to an instrument problem (drifting), as shown in Figure S3. Furthermore, the consistency between the arrival times of  $P_1$  and  $S_1$  phases of the Meinong earthquake and those of the  $P$  and  $S$  phases of the E2008 event (Fig. 6a) indicates that the hypocenter reported by CWB was the foreshock's hypocenter.

Figure 6b shows the waveforms after applying a 0.33 Hz low-pass filter, a common filter typically used in finite-fault inversion. The  $P_1$  and  $S_1$  phases become rather small, and the largest phase ( $S_2$ ) of the Meinong earthquake is  $\sim 7$  s later than the  $S$  phase of the E2008 earthquake. Therefore, in the case where the filter is applied, the Meinong earthquake seemingly appears to be a single event (the second event, mainshock) in the low-frequency band because the foreshock was buried due to the filtering. Several stations near the epicenter reported by CWB have the same characteristics as shown in Figure S4. This again suggests the benefit from the dense seismic network from unfiltered data to discover earthquake source complexity.

For determining the focal mechanism of the foreshock, we apply a grid-search technique to determine what focal solution can make  $S$ -wave amplitude ratios in three-component pairs (N/Z, N/E, and E/Z) of the synthetic waveforms ably consistent with the observed ones. We only analyze the unfiltered, clearly recorded  $S_1$  phases from 11 stations to the south. The synthetics are calculated by frequency–wavenumber ( $f$ - $k$ ) modeling (Zhu and Rivera, 2002) with an average 1D velocity model beneath these southern stations (H14-1D-S) calculated from the H14-3D model (Table 1). The searching ranges of strike, dip, and rake are  $250^\circ$  to  $300^\circ$ ,  $0^\circ$  to  $90^\circ$ , and  $-90^\circ$  to  $90^\circ$ , respectively. The best solution is given by strike/dip/rake = 275/20/15, which is close to the focal mechanism obtained by the RMT solution (276/22/20) (Lee *et al.*, 2016) rather than to the first-motion solution (263/15/–18) by the CWB (Fig. S5).

Because the focal mechanism and the hypocenter of the foreshock were determined, we simply compare the  $S_1$ -phase amplitudes of observation and synthetic in low frequencies ( $< 0.33$  Hz) from the MASB east component to estimate the moment magnitude for the foreshock. The synthetic of the  $S_1$  phase is calculated by the  $f$ - $k$  technique and the H14-1D-S

Table 1

The Layer Crustal Structure, H14-1D-S, for the Stations in the South

Layer	$H$ (km)	$V_P$ (km/s)	$V_S$ (km/s)	$\rho$ (g/cm <sup>3</sup> )	$Q_P$	$Q_S$
1	0.5	3.50	1.99	2.4	600	300
2	2.5	4.41	2.65	2.4	600	300
3	3.0	5.01	3.03	2.5	600	300
4	4.0	5.43	3.22	2.6	600	300
5	5.0	5.77	3.29	2.6	600	300
6	5.0	5.82	3.30	2.6	600	300
7	5.0	5.99	3.41	2.6	600	300
8	5.0	6.44	3.63	2.6	600	300
9	5.0	6.96	3.94	2.6	600	300
10	5.0	7.54	4.25	2.7	600	300
11	5.0	7.74	4.50	2.7	600	300
12	5.0	7.97	4.53	2.7	600	300
13	5.0	8.24	4.54	2.7	600	300

The average 1D velocity structure was determined from the H14-3D model (Huang *et al.*, 2014) in the area within longitude E120.60°–120.80° and latitude N22.50°–23.00° near the distribution of the stations in the south.

velocity model with a triangular source time function for 1 s duration. We assume that the contamination from the  $P_2$  phase was not significant. The reasonable moment magnitude of the foreshock is  $M_w$  5.5 (Ⓔ Fig. S6). Compared to the total moment of the  $M_w$  6.2 Meinong earthquake ( $M_0 = 2.5 \times 10^{18}$  N·m) determined by the RMT solution, the moment of the foreshock ( $M_0 = 2.2 \times 10^{17}$  N·m) was only ~10% of the total moment. It suggests that the waveforms in a low-frequency band might be dominated by the mainshock.

For the mainshock, we simply follow the solutions of the RMT solution because the waveforms in a low-frequency band should be dominated by the mainshock, due to the large difference in size of both events. The moment of the mainshock ( $2.3 \times 10^{18}$  N·m), which is calculated from the ratio of seismic moment against the foreshock, represents an  $M_w$  6.18 event. The best double-couple solution was 276/22/20 and 167/83/111, shown in Figures 1 and 5a.

## Discussion

### Two Independent Events or Two Asperities?

A common question raised for a complex source such as the Meinong earthquake is: Are these two events two asperities on the same fault or two independent events? To answer the question, we discuss the results from three different viewpoints. (1) The similarity of the focal mechanisms: two significantly different focal mechanisms may imply that two events have not occurred on the same fault plane. The result shown in the [Magnitudes and Focal Mechanisms of the Foreshock and the Mainshock](#) section, however, indicates that the focal solutions for both events have little difference. Hence, we are not able to make a conclusion from the focal mechanisms alone. (2) Spatial and temporal separations: consid-

erable temporal or spatial separations between the two events may suggest that the ruptures of these two events are disconnected. Our result shows that the centroids of the two events are ~12 km apart, based on the location solutions from the SSA method and the epicenter location proposed by the CWB. Temporally, the delay time between the foreshock origin and the mainshock centroid is 5.3 s. Combining the spatial and temporal relationships between the two events, and assuming the ruptures of the events are connected, the rupture velocity is ~2.31 km/s, which is slightly smaller than 0.8 times the  $S$ -wave velocity in the source region ( $V_S = 3.23$  km/s, H14-3D model) and 2.58 km/s and is consistent with the rupture speed determined by the backprojection technique (Jian *et al.*, 2017). Therefore, from the second viewpoint, this event could be considered as two independent sources or two asperities on the fault, whereas the evidence is not strong enough to draw a conclusion. (3) The characteristics of the local seismic waveforms: because of the fact that two clear  $P$ - and  $S$ -wave phase pairs are identified in the records from the southern stations (Figs. 3, 4, and 6), it might indicate that the two ruptures were interrupted (the foreshock and the mainshock discussed in the [Location of the Mainshock](#) section), or, at least, slips between both the rupture areas were tiny. In other words, the Meinong earthquake is more likely composed of two independent events from this point of view. Another evidence to support the two-independent-event hypothesis is that both events occurred in the same depth of 15 km but had a large horizontal separation of 12 km. To accommodate both events on a fault, we might need a nearly horizontal fault plane, which is inconsistent with the focal mechanism solutions.

It is intriguing to discuss how these two events were triggered at once. Further studies on earthquake dynamic triggering might help address this question. In addition, the interrupted rupture behavior between both events indicates that the strong directivity effect might be related to the mainshock only. In the [Observations and Modeling of the Pulse-Like Velocity Ground Motions](#) section, we will focus on the mainshock and simulate the waveform of the pulse-like velocity ground motions, which produced serious damage in the city of Tainan.

### Observations and Modeling of the Pulse-Like Velocity Ground Motions

Large pulse-like velocity ground motions related to the mainshock, which were identified at most stations near the city of Tainan (Ⓔ Fig. S7), were responsible for damaged building and fatalities. The pulse-like velocity ground motions recorded from those stations exhibit very large amplitude and narrow pulse widths (Fig. 7). The largest peak velocity was 101.2 cm/s with a period of 2 s, which appeared in the east component in the station W21B. This large velocity pulse with the short duration is similar to other velocity pulses recorded in the  $M_w$  6.7 Northridge and  $M_w$  6.6 San Fernando earthquakes (Cox and Ashford, 2002;

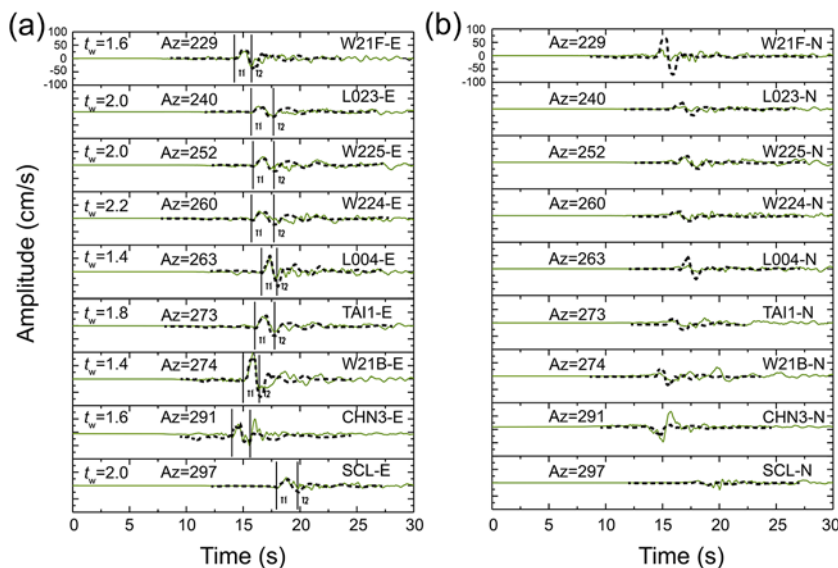


**Figure 7.** Observable (solid lines) and synthetic (dash lines) velocity waveforms in (a) east component and (b) north component for the stations in the city of Tainan. The durations of velocity pulses for the comparisons are marked in T1 and T2 markers. The best source duration used for each synthetic is shown on the trace. The color version of this figure is available only in the electronic edition.

Baker, 2007). We would like to directly simulate these large short-period velocity pulses without any filtering by considering the mainshock centroid information.

To model the velocity pulses shown in these stations, we consider an  $f$ - $k$  modeling (Zhu and Rivera, 2002) for an average 1D structure (H14-1D-W) around the city of Tainan extracted from the H14-3D model (Table 2), which includes

Table 2

The Crustal Structure, H14-1D-W, for the Stations in the City of Tainan

Layer	$H$ (km)	$V_p$ (km/s)	$V_s$ (km/s)	$\rho$ (g/cm <sup>3</sup> )	$Q_p$	$Q_s$
1	0.3	1.50	0.40	2.2	40	20
2	0.3	1.70	0.60	2.2	80	40
3	0.15	2.70	1.00	2.3	200	100
4	0.25	3.00	1.40	2.3	200	100
5	2.0	3.92	2.21	2.4	600	300
6	3.0	4.30	2.35	2.4	600	300
7	4.0	4.70	2.52	2.5	600	300
8	5.0	5.26	2.82	2.5	600	300
9	5.0	5.81	3.28	2.6	600	300
10	5.0	6.16	3.58	2.6	600	300
11	5.0	6.54	3.77	2.6	600	300
12	5.0	6.98	4.05	2.7	600	300
13	5.0	7.56	4.37	2.7	600	300
14	5.0	7.89	4.57	2.7	600	300
15	5.0	7.91	4.60	2.7	600	300
16	5.0	7.99	4.62	2.7	600	300

The average 1D velocity structure was determined from the H14-3D model (Huang *et al.*, 2014) in the area near the city of Tainan within longitude E120.10°–120.50° and latitude N22.75°–23.20°. The shallow structure (top four layers) was determined by microtremor analyses in the western plain of Taiwan described in Kuo *et al.* (2016). We consider the structure beneath Station CHY091, which is the nearest station of the city of Tainan, as the shallow structure used in this study.

a low  $S$ -wave velocity structure in the top 1000 m. The shallow structure was determined by microtremor analyses in the western plain of Taiwan described in Kuo *et al.* (2016). We extract a 1D structure right beneath station CHY091, a station that is closest to the city of Tainan, as the proxy for the shallowest part (depths < 1 km) of the structure used for computing synthetics.

We consider variable durations of triangular source time functions from 1.2 to 5.0 s and calculate the synthetic velocity waveforms for these stations using the seismic moment of  $M_0 = 2.3 \times 10^{18}$  N·m, or equivalent moment magnitude  $M_w$  6.18, as well as the focal mechanism of the RMT solution for the mainshock. We then compare the width of the velocity pulses between the synthetics and observations in the east–west component and determine the best apparent source duration for each station. The velocity pulse widths used for the

comparisons are shown in T1 and T2 markers in Figure 7a. The results indicate that we can explain most of the velocity pulses well in both horizontal components in the stations near the city of Tainan ( $AZ = 229^\circ$ – $279^\circ$ ) by a point source with a source time function of 1.4–2.2 s (Fig. 7a,b). The average source duration of these stations is 1.7 s. Furthermore, synthetics from the source parameters also explain the observations in the southern Station MASB ( $AZ = 163^\circ$ ) using a wider source time duration of 4.5 s (Fig. 8). It suggests a strong directivity effect toward the city of Tainan produced heavy damages, and it was due to the mainshock only. The results also indicate that the location, magnitude, and focal mechanism of the mainshock we estimated are reasonable.

#### Comparison of Two-Event Sources and the Finite-Fault Slip Model

The finite-fault slip distribution model from waveform inversion has become a useful tool to quickly reveal the slip distribution on the fault after an earthquake. Compared to the results from our two-event sources model, that analyzed unfiltered records, and the finite-fault slip model, that considered low-frequency geophysical records (Lee *et al.*, 2016), the largest source slip patterns and their strong directivity effect toward west of the Meinong earthquake are quite similar. The results from Lee *et al.* (2016) indeed revealed a large asperity to the north-northwest similar to the location of the mainshock (Fig. 9a). Both independent analyses of the present study and the finite-fault inversion using different data verified this source characteristic. However, the finite-fault centroid is 5 km deeper than the mainshock, as shown in Figure 9b. It may be related to an assumption of a north-dipping fault plane in the finite-fault study, where slip must

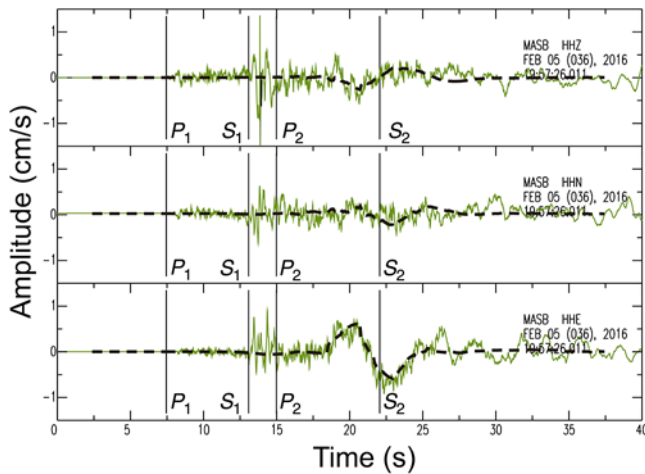


**Figure 8.** Observed (solid lines) and synthetic (dash lines) velocity waveforms for three components of the MASB station. The source time duration for the waveform simulations is 4.5 s. The synthetics were calculated for the H14-1D-S model. The color version of this figure is available only in the electronic edition.

occur on the presumed fault plane. Because the centroid location is in the north compared to the hypocenter at a depth of 14.6 km, it was consequently located at a depth of  $\sim 20$  km.

The consistency of the locations between the mainshock centroid and the largest slip asperities of the Meinong earthquake indicates that the improved SSA method is a powerful tool for determining the location of the source that generates large ground motions. Because it does not need precise source information (e.g., hypocenter and focal mechanism) of the targeted earthquake, the improved SSA method, rather than the finite-fault inversion, should be more efficient in determining the earthquake centroid location. It is worth combining the improved SSA method with the EEW system to demonstrate source centroid location and predict potential seismic hazard regions in real time for the public in the future.

Because a finite-fault waveform inversion is often applied to filtered data, the waveforms emitted by independent sources overlapped after filtering and, thus, yield a continuous slip distribution; therefore, the foreshock would be buried. The dense high-performance seismic array allows us to examine the earthquake sources through close observation. The result revealed in this study benefits from the dense high-quality strong-motion array. The low-cost seismometer for the purpose of EEW is surprisingly well behaved, giving close observations to earthquake sources with less distortion of waveforms from filtering. It is indeed worthy to note using the low-cost strong-motion array for the future understanding of earthquake sources, especially linked to earthquake engineering.

### Conclusions

Using the seismic records from the local dense networks without any filter, we recognize that the Meinong earthquake

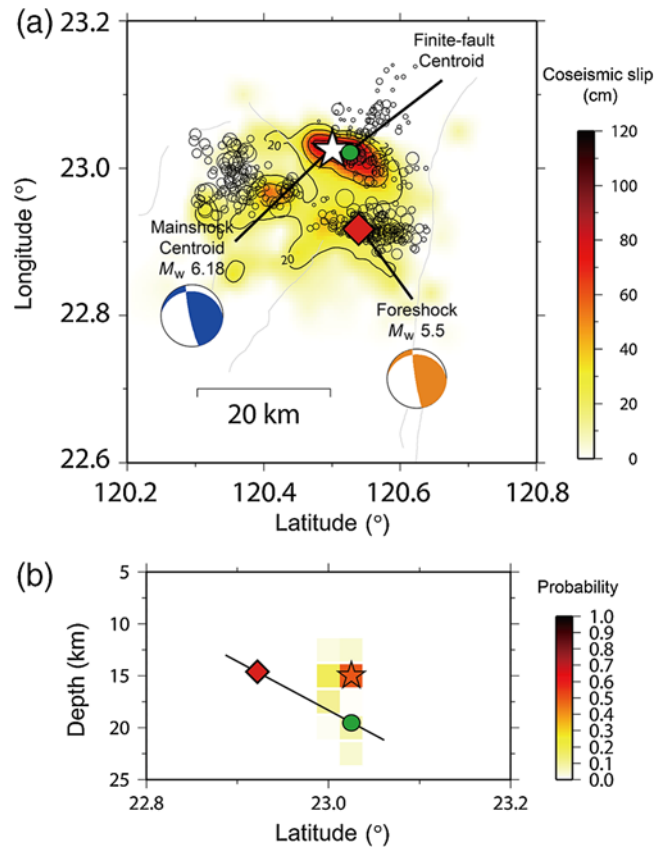


**Figure 9.** (a) Comparison of the two-source model described in the present study and the coseismic slip distribution described in the Lee *et al.* (2016) study (counters). Open circles indicate the aftershocks of the 2016 Meinong earthquake. The star and diamond are the locations of the mainshock centroid (SSA) and epicenter (CWB), respectively. The solid circle denotes the centroid from the finite-fault inversion. The color scale indicates the coseismic slip determined by the finite-fault inversion. (b) Comparison of the mainshock centroid and the finite-fault centroid. The line indicates the assumed fault plane used in the finite-fault inversion. The diamond, circle, and open star demonstrate the hypocenter of the foreshock, the finite-fault centroid, and the mainshock centroid, respectively. The color scale indicates the probability of the mainshock centroid. The color version of this figure is available only in the electronic edition.

can be separated into an  $M_w$  5.5 foreshock and an  $M_w$  6.18 mainshock. The  $P$ - and  $S$ -wave phases of the foreshock ( $P_1$  and  $S_1$ ) and the mainshock ( $P_2$  and  $S_2$ ) were identified clearly in the travel-time curves for the southern stations, which is backward from the rupture direction. The time delay of the mainshock centroid is  $\sim 5.3$  s. The location of the foreshock is at the hypocenter estimated by the CWB. We located the mainshock centroid by applying the modified SSA technique. The result indicates that the mainshock centroid occurred 12.3 km north-northwest of the foreshock where there is a blank zone of the aftershocks, which is consistent with the results of the finite-fault study. However, the depth of the mainshock was 15 km, which is shallower than the centroid location determined by finite-fault inversion. The focal mechanism of the foreshock is 276/22/20 in strike/dip/rake,

which is similar to the mainshock. Because of the clear identification of the phases in dense strong-motion stations, we believe that the foreshock and the mainshock were individual earthquakes rather than two asperities on a fault plane. This nonnegligible foreshock for the epicenter region would be buried once we apply a low-pass filter on data processing, commonly used in source properties studies. The pulse-like velocity ground motions, responsible for the extensive damage, could be explained solely from a single source in the mainshock, which was well modeled. The combination of the close-in distance, the strong directivity from the mainshock, and the site effect resulted in large velocity pulses that struck the city of Tainan, causing the disastrous damage. Using a dense seismic network as a seismic array helps us delineate the earthquake sources directly and provides more delicate information for future understanding of earthquake dynamic triggering. In the future, with more advanced development of low-cost seismometers, the seismic array method could become an important tool in deciphering earthquake source complexity. The experience from this Meinong earthquake could be a classic case study.

### Data and Resources

The strong-motion waveform records used in this study were obtained from the National Taiwan University (NTU), the Institute of Earth Sciences (IES) of Academia Sinica, and the Central Weather Bureau (CWB). The  $P$ -alert records used in this study are available to the public and can be downloaded from the NTU cloud disk (<https://www.space.ntu.edu.tw/navigate/s/5CDFA7C2CFD7487FB84E2CE3F7376C33Q QY>, last accessed March 2016). The strong-motion records from IES and CWB used in this study can be obtained upon request from IES and CWB. The damage records used in this study are at <http://data.tainan.gov.tw/dataset/0206-earthquake/resource/476c935a-1611-40f0-ae46-0b53fd588c1f> (last accessed June 2017). The Broadband Array in Taiwan for Seismology (BATS) solution is available at <http://bats.earth.sinica.edu.tw> (last accessed June 2017), and the Global Centroid Moment Tensor (CMT) solution is maintained at <http://www.globalcmt.org/CMTsearch.html> (last accessed June 2017). The CWB website can be accessed at <http://www.cwb.gov.tw/eng/index.htm> (last accessed March 2016). The Seismic Analysis Code (SAC) is available at <http://ds.iris.edu/files/sac-manual/> (last accessed July 2016). The Frequency-wavenumber ( $f$ - $k$ ) synthetic seismogram package is available at <http://www.eas.slu.edu/People/LZhu/home.html> (last accessed June 2017).

### Acknowledgments

The authors appreciate the helpful comments from Associate Editor Michel Bouchon, three reviewers, Hiroo Kanamori, Victor C. Tsai, and Zachary E. Ross, who helped us improve this article. The authors thank Hsin-Hua Huang at the Institute of Earth Sciences (IES), Academia Sinica, Taiwan, for providing Taiwan 3D velocity structure. Thanks to the Central Weather Bureau (CWB) for providing the Real-Time Data (RTD) records

and source parameters, including earthquake location and focal mechanism, of the Meinong earthquake. This research was supported by the Taiwan Earthquake Research Center (TEC), funded through the Ministry of Science and Technology (MoST) with Grant Numbers MOST 103-2628-M-001-004-MY3 and MOST 106-2119-M-008-006. T.-R. A. Song is supported by Natural Environment Research Council (NERC) Grant Number NE/P001378/1. The TEC Contribution Number for this article is 00140.

### References

- Baker, J. W. (2007). Quantitative classification of near-fault ground motions using wavelet analysis, *Bull. Seismol. Soc. Am.* **97**, no. 5, 1486–1501, doi: [10.1785/0120060255](https://doi.org/10.1785/0120060255).
- Cox, K. E., and S. A. Ashford (2002). Characterization of large velocity pulses for laboratory testing, *PEER Report 2002/22*, Pacific Earthquake Engineering Research Center, University of California, Berkeley, California.
- Duputel, Z., V. C. Tsai, L. Rivera, and H. Kanamori (2013). Using centroid time-delays to characterize source durations and identify earthquakes with unique characteristics, *Earth Planet. Sci. Lett.* **374**, 92–100, doi: [10.1016/j.epsl.2013.05.024](https://doi.org/10.1016/j.epsl.2013.05.024).
- Hall, J. F., T. H. Heaton, M. W. Halling, and D. J. Wald (1995). Near-source ground motion and its effects on flexible buildings, *Earthq. Spectra* **11**, no. 4, 569–605.
- Heaton, T. H., J. F. Hall, D. J. Wald, and M. W. Halling (1995). Response of high-rise and base-isolated buildings to hypothetical  $M_w$  7.0 blind thrust earthquake, *Science* **267**, 206–211.
- Huang, H.-H., Y.-M. Wu, C.-H. Chang, S.-J. Lee, T.-M. Chang, and H.-H. Hsieh (2014). Joint  $V_p$  and  $V_s$  tomography of Taiwan: Implications for subduction-collision orogeny, *Earth Planet. Sci. Lett.* **392**, 177–191.
- Jian, P.-R., S.-H. Hung, L. Meng, and D. Sun (2017). Rupture characteristics of the 2016 Meinong earthquake revealed by the backprojection and directivity analysis of teleseismic broadband waveforms, *Geophys. Res. Lett.* **44**, 3545–3553, doi: [10.1002/2017GL072552](https://doi.org/10.1002/2017GL072552).
- Kan, C.-W., H. Kao, G.-B. Ou, R.-Y. Chen, and C.-H. Chang (2010). Delineating the rupture planes of an earthquake doublet using source-scanning algorithm: Application to the 3 March 2005 Ilan doublet, northeast Taiwan, *Geophys. J. Int.* **182**, 956–966.
- Kanamori, H., L. Ye, B.-S. Huang, H.-H. Huang, S.-J. Lee, W.-T. Liang, Y.-Y. Lin, K.-F. Ma, Y.-M. Wu, and T.-Y. Yeh (2016). A strong-motion hot spot of the 2016 Meinong, Taiwan, earthquake ( $M_w = 6.4$ ), *Terr. Atmos. Ocean. Sci.* **28**, 637–650, doi: [10.3319/TAO.2016.10.07.01](https://doi.org/10.3319/TAO.2016.10.07.01).
- Kao, H., and S.-J. Shan (2004). The source-scanning algorithm: Mapping the distribution of seismic sources in time and space, *Geophys. J. Int.* **157**, 589–594.
- Kao, H., and S.-J. Shan (2007). Rapid identification of earthquake rupture plane using source-scanning algorithm, *Geophys. J. Int.* **168**, 1011–1020.
- Kao, H., C.-W. Kan, R.-Y. Chen, C.-H. Chang, A. Rosenberger, T.-C. Shin, P.-L. Leu, K.-W. Kuo, and W.-T. Liang (2012). Locating, monitoring, and characterizing typhoon-induced landslides with real-time seismic signals, *Landslides* **9**, 557–563, doi: [10.1007/s10346-012-0322-z](https://doi.org/10.1007/s10346-012-0322-z).
- Kao, H., K. Wang, R.-Y. Chen, I. Wada, J. He, and S. D. Malone (2008). Identifying the rupture plane of the 2001 Nisqually, Washington, earthquake, *Bull. Seismol. Soc. Am.* **98**, 1546–1558.
- Kuo, C.-H., C.-T. Chen, C.-M. Lin, K.-L. Wen, J.-Y. Huang, and S.-C. Chang (2016). S-wave velocity structure and site effect parameters derived from microtremor arrays in the western plain of Taiwan, *J. Asian Earth Sci.* **128**, 27–41, doi: [10.1016/j.jseae.2016.07.012](https://doi.org/10.1016/j.jseae.2016.07.012).
- Lee, S.-J., T.-Y. Yeh, and Y.-Y. Lin (2016). Anomaly large ground shaking caused by constructive source rupture and wave propagation effects during the 6 February 2016 Meinong, Taiwan, M 6.6 earthquake, *Seismol. Res. Lett.* **87**, no. 6, 1319–1326, doi: [10.1785/0220160082](https://doi.org/10.1785/0220160082).
- Liao, Y.-C., H. Kao, A. Rosenberger, S.-K. Hsu, and B.-S. Huang (2012). Delineating complex spatiotemporal distribution of earthquake after-shocks: An improved source-scanning algorithm, *Geophys. J. Int.* **189**, 1753–1770, doi: [10.1111/j.1365-246X.2012.05457.x](https://doi.org/10.1111/j.1365-246X.2012.05457.x).

- Shahi, S. K., and J. W. Baker (2011). An empirically calibrated framework for including the effects of near-fault directivity in probabilistic seismic hazard analysis, *Bull. Seismol. Soc. Am.* **101**, no. 2, 742–755, doi: [10.1785/0120100090](https://doi.org/10.1785/0120100090).
- Somerville, P. G. (2003). Magnitude scaling of the near fault rupture directivity pulse, *Phys. Earth Planet. In.* **137**, 201–212.
- Somerville, P. G., N. F. Smith, R. W. Graves, and N. A. Abrahamson (1997). Modification of empirical strong ground motion attenuation relations to include the amplitude and duration effects of rupture directivity, *Seismol. Res. Lett.* **68**, no. 1, 199–222.
- Wu, Y.-M., D.-Y. Chen, T.-L. Lin, C.-Y. Hsieh, T.-L. Chin, W.-Y. Chang, W.-S. Li, and S. H. Ker (2013). A high-density seismic network for earthquake early warning in Taiwan based on low cost sensors, *Seismol. Res. Lett.* **84**, 1048–1054, doi: [10.1785/0220130085](https://doi.org/10.1785/0220130085).
- Wu, Y.-M., W.-T. Liang, H. Mittal, W.-A. Chao, C.-H. Lin, B.-S. Huang, and C.-M. Lin (2016). Performance of a low-cost earthquake early warning system (*P*-alert) during 2016  $M_L$  6.4 Meinong (Taiwan) earthquake, *Seismol. Res. Lett.* **87**, no. 5, doi: [10.1785/0220160058](https://doi.org/10.1785/0220160058).
- Zhu, L., and L. A. Rivera (2002). A note on the dynamic and static displacements from a point source in multilayered media, *Geophys. J. Int.* **148**, 619–627, doi: [10.1046/j.1365-246X.2002.01610.x](https://doi.org/10.1046/j.1365-246X.2002.01610.x).
- Institute of Earth Sciences  
Academia Sinica  
128, Section 2, Academia Road  
Nangang District  
Taipei 11529, Taiwan  
yenyulin@caltech.edu  
(Y.-Y.L., T.-Y.Y., S.-J.L., B.-S.H.)
- Department of Earth Sciences  
National Central University  
No. 300, Jhongda Road  
Jhongli District  
Taoyuan 32001, Taiwan  
(K.-F.M.)
- Department of Earth Sciences  
University College London  
Gower Street  
London WC1E 6BT, United Kingdom  
(T.-R.A.S.)
- Department of Geosciences  
National Taiwan University  
No. 1, Section 4, Roosevelt Road  
Taipei 10617, Taiwan  
(Y.-M.W.)

Manuscript received 4 June 2017;  
Published Online 2 January 2018